


## Two-dimensional surface phase diagram of a multicomponent perovskite oxide: $\text{La}_{0.8}\text{Sr}_{0.2}\text{MnO}_3(110)$

Giada Franceschi , Michael Schmid , Ulrike Diebold, and Michele Riva <sup>\*</sup>  
Institute of Applied Physics, TU Wien, Wiedner Hauptstraße 8–10/E134, 1040 Wien, Austria

 (Received 19 September 2020; revised 27 May 2021; accepted 30 August 2021; published 24 September 2021)

The many surface reconstructions of (110)-oriented lanthanum strontium manganite ( $\text{La}_{0.8}\text{Sr}_{0.2}\text{MnO}_3$ , LSMO) were followed as a function of the oxygen chemical potential ( $\mu_{\text{O}}$ ) and the surface cation composition. Decreasing  $\mu_{\text{O}}$  causes Mn to migrate across the surface, enforcing phase separation into *A*-site-rich areas and a variety of composition-related, structurally diverse *B*-site-rich reconstructions. The composition of these phase-separated structures was quantified with scanning tunneling microscopy, and these results were used to build a two-dimensional phase diagram of the LSMO(110) equilibrium surface structures.

DOI: [10.1103/PhysRevMaterials.5.L092401](https://doi.org/10.1103/PhysRevMaterials.5.L092401)

The surfaces of oxide materials, both in their bulk form and as (ultra)thin films, are rarely bulk terminated. Instead, they form a multitude of diverse and complex structural configurations as a function of their oxygen content [1–6], their cation composition (for multielement materials) [7,8], and, in the case of metal-supported ultrathin films, the support itself [3,5]. This manifold of phases is determined by a delicate interplay between polarity compensation [9], variability of the oxidation state of the metal atoms as a function of the oxygen chemical potential ( $\frac{1}{2}\mu_{\text{O}_2}$  [10,11], henceforth  $\mu_{\text{O}}$  for simplicity), strain and defect-formation energies [12], and, depending on the preparation conditions, kinetic effects [5].

Mapping out the parameter space of the equilibrium surface phases of metal oxides is important from both, fundamental, and application standpoints: The many available studies on binary oxides and the few pioneering works on perovskite oxides ( $\text{ABO}_3$ ) prove that each surface reconstruction has unique properties and a potential for applications, owing to the specific arrangement, coordination, and electronic structure of its topmost atoms [13–20]. Building quantitative phase diagrams for the surface phases of metal oxides is thus essential to determine their stability limits and potential areas of application. In other words, with an established phase diagram one can pick the appropriate experimental conditions to obtain specific surface phases.

The surfaces of perovskite oxides are particularly relevant for many emerging and established technologies [21–24], and yet they are scarcely explored. One prominent example is lanthanum strontium manganite (LSMO). Owing to its many and diverse physical properties (among others, half metallicity, colossal magnetoresistance, metal-insulator transition, anti/ferromagnetic to paramagnetic transitions, high electronic conductivity at elevated temperatures), LSMO is used in widely different fields, e.g., spintronics [25–27], catalysis [28,29], energy conversion [30,31], and various thin-film technologies [32–34]. In all cases, the role of LSMO surfaces and interfaces is key, which calls for a comprehensive under-

standing of the equilibrium surface phases of LSMO at the local (i.e., atomic) level. This must be performed as a function of both the cation and the oxygen concentrations (the latter depends on the value of  $\mu_{\text{O}}$  at which the surface is treated): Both parameters induce structural phase transitions [35–37], influence the physical properties named above [36], affect the performance of LSMO-based devices [38–41], and cause emergent phenomena in LSMO thin films [42]. To date, however, there exists no experimental investigation that simultaneously maps out the equilibrium surface phases of LSMO (nor of any other multielement oxide) as a function of the cation composition and  $\mu_{\text{O}}$ . The few studies available have unveiled that perovskite oxide surfaces typically consist of *B*-site-rich structures made of one or two atomic layers of differently linked polyhedra [43,44], and have focused on their relation to the *A* : *B* cation ratio at the surface. In some cases, quantitative compositional relations between the different structures have been established [7,8,45,46]. On the other hand, some theoretical works have explored the phase diagram of  $\text{LaMnO}_3$  surfaces as a function of both the cation composition and  $\mu_{\text{O}}$  [47–49]. However, these studies most often assume bulk-truncated terminations, which, as demonstrated here, are an oversimplification of reality.

This Letter pushes the experimental characterization of perovskite oxide surfaces, by investigating the effect of the cation composition and  $\mu_{\text{O}}$  on the local surface properties of (110)-oriented LSMO. Single-crystalline films of  $\text{La}_{0.8}\text{Sr}_{0.2}\text{MnO}_3$  were grown on Nb-doped  $\text{SrTiO}_3(110)$  substrates by pulsed laser deposition (PLD) ( $\approx 100$  nm, 700 °C, 1 Hz, 2.2 J/cm<sup>2</sup>,  $4 \times 10^{-2}$  mbar O<sub>2</sub>) [8]. Their surfaces were investigated in an ultrahigh vacuum (UHV) surface-science setup attached to the PLD chamber, equipped with scanning tunneling microscopy (STM), low-energy electron diffraction (LEED), x-ray photoelectron spectroscopy (XPS), and low-energy He<sup>+</sup>-ion scattering (LEIS) (for details about the experimental methods, see Refs. [8,50], and Sec. S1 in the Supplemental Material [51]). Previous studies have shown that these films exhibit composition-related surface reconstructions at 700 °C and 0.2 mbar O<sub>2</sub>, and have established the differences in cation coverages between them [8]. These

<sup>\*</sup>Corresponding author: [riva@iap.tuwien.ac.at](mailto:riva@iap.tuwien.ac.at)

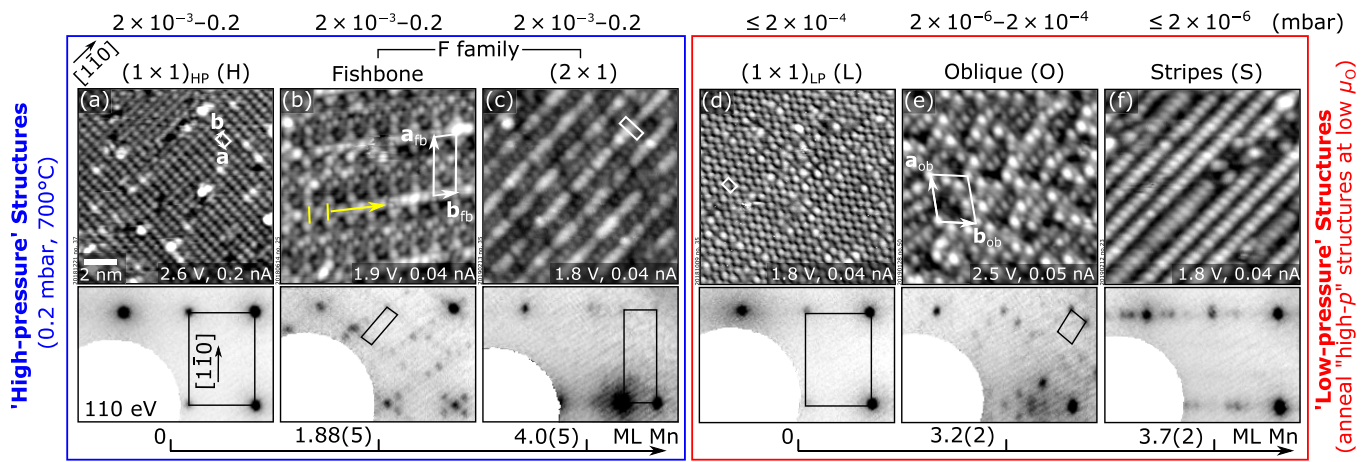


FIG. 1. Equilibrium surface structures of LSMO(110). Top:  $12 \times 12 \text{ nm}^2$  STM images; bottom: LEED.  $\text{O}_2$  pressure ranges (millibar) where each reconstruction is stable at  $700^\circ\text{C}$  are reported at the top. (a)–(c) High-pressure (HP) structures, obtained by depositing Mn or La in PLD plus  $\text{O}_2$  annealing [8]. (d)–(f) Low-pressure (LP) structures, formed by annealing the HP structures at low pressure. The  $(1 \times 1)_{\text{HP/LP}}$  surfaces have the same cation composition. Each structure is identified at the top by its superstructure periodicity and/or by a descriptive, shorthand label used in the text. Relative compositions are given in the bottom axes [1 ML is the number of Mn atoms in an  $(\text{AMnO})_2$  plane of LSMO(110),  $4.64 \times 10^{14} \text{ cm}^{-2}$ ].

phases, here referred to as “high pressure” (HP), are shown for reference at the left-hand side of Fig. 1, and are described in detail in Sec. S2 [51]. The current work is based on the behavior of the HP phases over a wide range of  $\mu_{\text{O}}$  values (between  $\approx -2.1 \text{ eV}$  and  $\approx -1.4 \text{ eV}$ , corresponding to annealing between UHV and  $0.2 \text{ mbar O}_2$  at  $700^\circ\text{C}$ ): When decreasing  $\mu_{\text{O}}$  (i.e., at more reducing conditions), the surface phase-separates, exposing new “low-pressure” (LP) structures. These are collected at the right-hand side of Fig. 1, and are described in detail in Sec. S3 [51]. Their relative compositions, as derived in this Letter, are reported in the bottom axis in terms of monolayers (ML) of Mn.

After exploring the behavior of the HP structures with decreasing  $\mu_{\text{O}}$  and the process of phase separation, this Letter provides a strategy, based on STM, to organize the equilibrium surface phases of LSMO(110) (both HP and LP) in a quantitative two-dimensional (2D) phase diagram as a function of cation composition and  $\mu_{\text{O}}$ . The phase diagram outlines the stability regions for the single-, two-, and three-phase equilibria observed at given combinations of cation compositions and  $\mu_{\text{O}}$ .

First, it is useful to consider the behavior of the A-site-rich  $(1 \times 1)_{\text{HP}}$  of Fig. 1(a) with decreasing  $\mu_{\text{O}}$ . This structure stays unaltered upon annealing at  $700^\circ\text{C}$  and  $2 \times 10^{-3} \text{ mbar} \leq p_{\text{O}_2} \leq 0.2 \text{ mbar}$ , but transforms into the  $(1 \times 1)_{\text{LP}}$  of Fig. 1(d) at lower pressures (down to UHV). The  $(1 \times 1)_{\text{LP}}$  is characterized by the same periodicity as its HP counterpart, and the same cation composition [see LEIS data in Fig. S1(b) [51]]. However, it displays a glide plane that is not present in the  $(1 \times 1)_{\text{HP}}$ , and possesses a smaller oxygen content [see Fig. S1(b) [51]]. The  $(1 \times 1)_{\text{HP}}$  undergoes this transition with  $\mu_{\text{O}}$  regardless of whether it is the only phase or if it coexists with other phases at the surface (see also Sec. S2 [51]).

The other HP phases of LSMO(110) behave differently than the  $(1 \times 1)_{\text{HP}}$  with decreasing  $\mu_{\text{O}}$ , as shown below. These monophase structures are more Mn rich and belong to a different family with respect to the  $(1 \times 1)_{\text{HP}}$ : Small changes in the

Mn content induce a continuous evolution between the fishbone reconstruction and the  $(2 \times 1)$  of Figs. 1(b) and 1(c) [8]. They are henceforth referred to as HP, “Mn-rich” phases, or as reconstructions belonging to the fishbone (F) family. The qualitative behavior of the F family with decreasing  $\mu_{\text{O}}$  is exemplified by Fig. 2, showing the evolution of the monophase fishbone phase of Fig. 1(b), initially prepared at  $0.2 \text{ mbar}$  and  $700^\circ\text{C}$ . When decreasing  $p_{\text{O}_2}$  to  $2 \times 10^{-3} \text{ mbar}$  at  $700^\circ\text{C}$ , small  $(1 \times 1)_{\text{HP}}$  areas appear (orange in Fig. 2). These patches become larger as  $\mu_{\text{O}}$  decreases, and change their atomic structure to  $(1 \times 1)_{\text{LP}}$ . Meanwhile, the remaining fishbone-reconstructed surface undergoes a minor structural change: The small features highlighted by the short yellow lines in Figs. 2(a<sub>2</sub>) and 2(b<sub>2</sub>) orient closer to the  $[1\bar{1}0]$  direction, an indication of a slight Mn enrichment [8]. Between  $1 \times 10^{-4}$  and  $5 \times 10^{-6} \text{ mbar}$  [Fig. 2(c)], larger  $(1 \times 1)_{\text{LP}}$  patches form, while the remaining surface exposes the oblique structure of Fig. 1(e). Below  $5 \times 10^{-6} \text{ mbar}$  and down to UHV [Fig. 2(d)], even larger  $(1 \times 1)_{\text{LP}}$  patches are observed, while the remaining areas exhibit the stripes of Fig. 1(f). Importantly, the process is reversible: STM confirms that the initial surface is regained when annealing back at high  $p_{\text{O}_2}$ .

Quantifying the  $(1 \times 1)_{\text{HP/LP}}$  areal coverages at each step of the phase separation with STM [Fig. 3(a)] allows one to determine the composition of the LP Mn-rich structures, as shown below. Since the following discussion focuses on relative cation compositions, which is the same on  $(1 \times 1)_{\text{HP}}$  and  $(1 \times 1)_{\text{LP}}$ , these will be henceforth referred to simply as  $(1 \times 1)$ , disregarding their different atomic structure and oxygen content. In Fig. 3(a), orange symbols represent the evolution of a monophase  $(1 \times 1)$ . As this surface does not phase separate, the plot with  $\mu_{\text{O}}$  shows a constant  $(1 \times 1)$  area fraction of 100%. Solid, black symbols correspond to the experiment of Fig. 2: Decreasing  $\mu_{\text{O}}$  produces increasingly larger  $(1 \times 1)$  areas. Mn-richer starting surface compositions (gray) exhibit the same trend, albeit with a smaller slope: Mn-richer surfaces form less of the Mn-poorer  $(1 \times 1)$  areas.

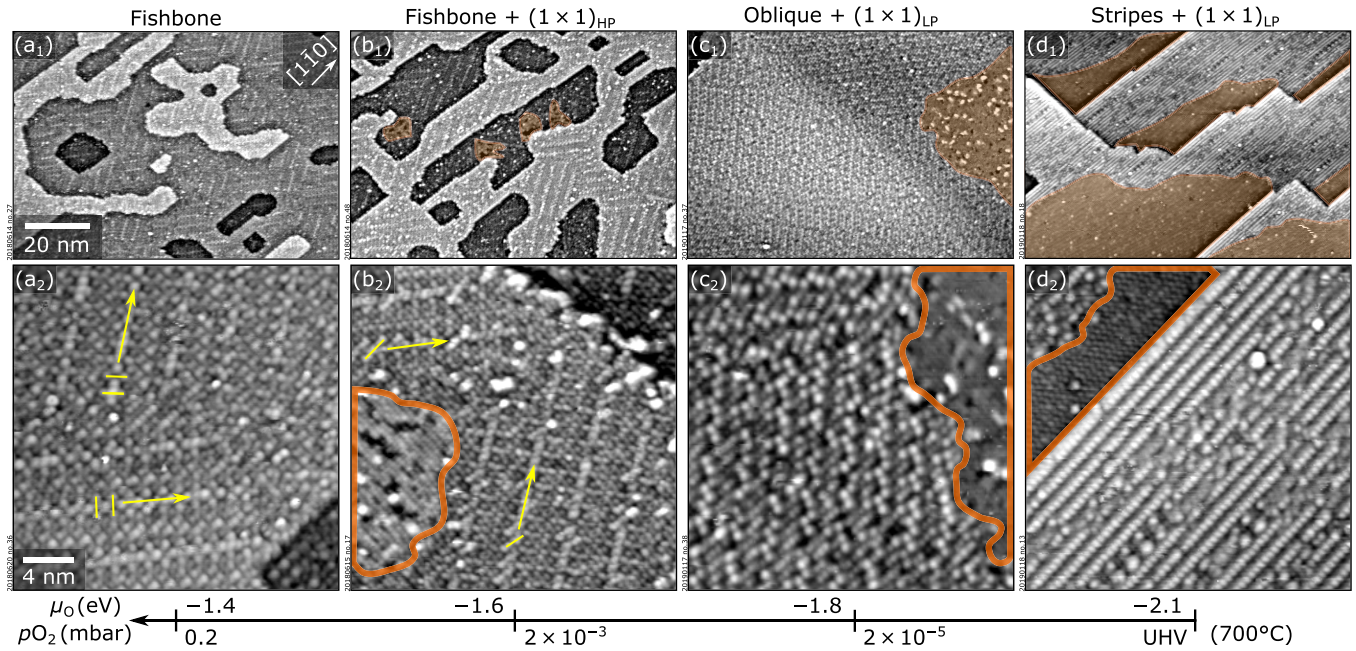


FIG. 2. Evolution of the monophase fishbone surface upon annealing at increasingly reducing conditions. (a<sub>1</sub>)–(d<sub>1</sub>), (a<sub>2</sub>)–(d<sub>2</sub>) STM images ( $100 \times 70 \text{ nm}^2$ , and  $26 \times 26 \text{ nm}^2$ , respectively). (a) Monophase fishbone surface. (b) After annealing at  $2 \times 10^{-3}$  mbar, small  $(1 \times 1)_{\text{HP}}$  patches appear (orange), and small structural changes occur in the fishbone. (c) Annealing at  $2 \times 10^{-5}$  mbar produces  $(1 \times 1)_{\text{LP}}$  areas, and transforms the remaining surface into the oblique structure of Fig. 1(e). (d) UHV annealing enlarges the  $(1 \times 1)_{\text{LP}}$  areas, and transforms the remaining surface into the stripes of Fig. 1(f). The process is reversible.

(The only difference for Mn-richer F surfaces is that a mixture of fishbone and oblique phases appears in the  $10^{-3}$ – $10^{-4}$  mbar pressure range.)

Importantly, for a given initial Mn concentration, the same phases with the same quantitative coverages are observed under the same value of  $\mu_{\text{O}}$ , obtained from different combinations of temperature and  $p_{\text{O}_2}$  [dashed oval in Fig. 3(a)]. This indicates that the observed surface structures are equilibrium phases, and that the phase separation is not kinetically limited.

What drives the phase separation? One can rule out evaporation of cations (due to the reversibility), as well as cation diffusion to or from the bulk (at the employed conditions, cations can travel in bulk LSMO at most one atomic layer [52]): The phase separation thus occurs by mass transport across the surface. The proposed mechanism, sketched in Fig. 3(c), is that Mn travels across the surface and exposes the very stable, Mn-poor  $(1 \times 1)$  phase, while enriching the remaining areas. Several facts support this scenario: (i) The average surface cation composition stays constant, as indicated by the reversibility of the process, and from the XPS data of Fig. 3(b): These show that the intensity ratios of selected core level peaks have no trend with  $\mu_{\text{O}}$ . Given the sensitivity of XPS to the cation composition of monophase LSMO(110) structures [8], the absence of a trend indicates that the average surface composition is conserved; (ii) the LEIS data of Fig. 3(d), showing that the monophase oblique phase is Mn-richer than the monophase fishbone; (iii) the decreasing trend of the O  $1s$ –Mn  $2p_{3/2}$  peak separation with decreasing  $\mu_{\text{O}}$  (see Sec. S5 [51]), consistent with a decreasing oxidation state of Mn in the LP, Mn-rich areas [8].

It is too early to tell whether the  $\mu_{\text{O}}$ -dependent phase separation witnessed for LSMO(110) can be generalized to the class of perovskite oxides, mostly due to the current lack of knowledge on their surfaces. The only other perovskite oxide whose surfaces have been investigated in significant depth, SrTiO<sub>3</sub>, shows a phase separation among stable surface structures with different  $A : B$  ratio [53], but not as a function of  $\mu_{\text{O}}$  [12]. This is presumably because SrTiO<sub>3</sub> does not possess the same flexibility in the oxidation state of the  $B$  cation as LSMO [54–56], and because of the small tendency to form oxygen vacancies in the common Nb-doped specimens [18]. Materials with easily reducible cations are expected to behave similarly to LSMO(110): After all, structurally complex  $B$ -site-rich surface reconstructions that depend on both cation and anion compositions seem to be a general trait of perovskite oxides [6,43,44,57]. Moreover, an AO termination was preferentially exposed at reducing conditions also in another manganite [58], and a similar effect was predicted for LSMO(001) [49].

The remarkable diversity of the surface phases of perovskite oxides calls for methods capable of accessing and controlling their local surface properties as a function of different cation and anion compositions. Here, such a method is showcased for LSMO(110). Through an application of the lever and Gibbs' phase rules, its surface phases can be organized in a 2D phase diagram as a function of  $\mu_{\text{O}}$  and the excess of Mn at the surface,  $\Delta\chi_{\text{Mn}}$  [Figs. 4(b) and S5(a) [51]].

Section S4 [51] details the assumptions underlying the construction of the phase diagram. It shows that the most natural axes are  $\mu_{\text{O}}$ ,  $\Delta\chi_{\text{Mn}}$ , and temperature, and argues that



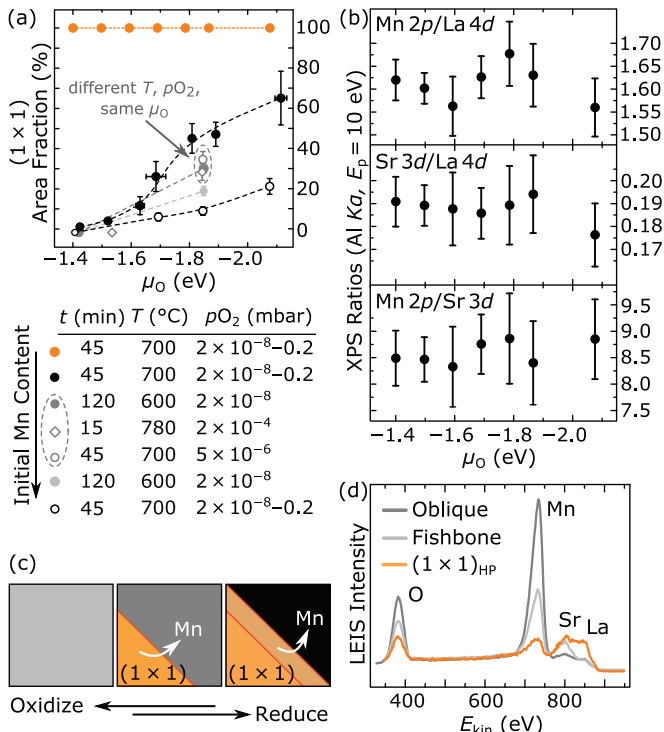


FIG. 3. (a) STM quantification of  $(1 \times 1)$  area fractions during the phase separation of LSMO(110) surfaces, starting from different high-pressure phases. Each point averages over 10–12 images acquired on  $300 \times 300 \text{ nm}^2$  on different sample spots. Orange: Initially  $(1 \times 1)_{\text{HP}}$ . Solid black circles: Initially monophase fishbone (Fig. 2). Other symbols: Initial surfaces between fishbone and  $(2 \times 1)$ . Dashed oval: Different  $(T, p_{\text{O}_2})$  combinations, equivalent to the same  $\mu_{\text{O}}$ . The table indicates the annealing parameters for each data point. Lines are a guide for the eye. (b) XPS intensity ratios have no trend with  $\mu_{\text{O}}$  within the error bars (the data correspond to the experiment of Fig. 2, and are representative of all experiments). (c) Proposed mechanism: Mn travels across the surface to expose  $(1 \times 1)$  and form new Mn-richer structures, preserving the overall cation composition. (d) LEIS spectra of different monophase surfaces. Differences in the relative Sr-to-La signals are related to different sample histories, and do not affect the overall appearance of the corresponding reconstructions [8] (see also Secs. S2 and S4A [51]).

the latter has a negligible influence. This is why the surface phase diagram of LSMO(110) can be fully represented in two dimensions as in Fig. 4(b), as a function of  $\mu_{\text{O}}$  and  $\Delta\chi_{\text{Mn}}$ . General considerations about the Gibbs' phase rule (Sec. S4 [51]) then let one predict that, at equilibrium, the LSMO(110) surface can host one, two, three, or four distinct, coexisting phases. This is consistent with the experimental evidence, as exemplified by the monophase fishbone in Fig. 2(a), the simultaneous presence of  $(1 \times 1)$  and LP Mn-rich structures in Figs. 2(b)–2(d), and the three-phase equilibria in Fig. S5 [51]. Four distinct phases were never observed, as expected from the rarity of parameter combinations at which they should appear.

To construct the phase diagram, one has to account for the evolution of phase-separated surfaces with  $\mu_{\text{O}}$ : Mn-rich

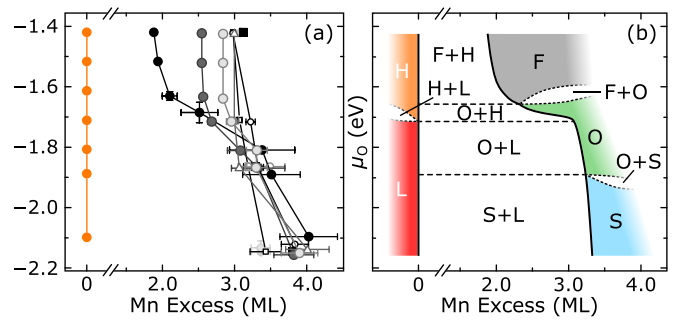


FIG. 4. Experimental 2D surface phase diagram of LSMO(110). (a) Evolution of the composition of different phases of LSMO(110) with decreasing  $\mu_{\text{O}}$ , as derived from the data in Fig. 3(a). (b) Corresponding model. Reconstructions are identified by labels, indicating single and multiphase regions (selected STM images are shown in Sec. S4 [51]). H, L:  $(1 \times 1)_{\text{HPLP}}$ . F: Fishbone family. O: Oblique. S: Stripes.

areas undergo changes in their composition and areal coverage (Figs. 2 and 3). As discussed in Sec. S4 [51], the composition of these evolving Mn-rich areas can be obtained from the  $(1 \times 1)$  coverages in Fig. 3(a) by applying the lever rule, and considering that the total number of surface cations is conserved. Figure 4(a) shows the outcome. The leftmost curve represents the evolution of the initially monophase  $(1 \times 1)$  surface, whose cation composition is constant. The solid black circles follow the composition of the Mn-rich areas of an initially monophase fishbone surface (Fig. 2) that phase-separates with decreasing  $\mu_{\text{O}}$ . The other curves correspond to initially monophase Mn-richer F structures: They remain vertical until phase separation sets in.

The results in Fig. 4(a) are the basis to construct the surface phase diagram in Figs. 4(b) and S5(a) [51]. The position of the left-hand-side boundary of the stability region of the LP, Mn-rich phases [solid line in Fig. 4(b)] is obtained by taking the leftmost points, at given  $\mu_{\text{O}}$ , among all the curves in Fig. 4(a); it is further refined using as constraints the experimentally determined phase assemblages (i.e., which phases appear at all combinations of surface compositions and  $\mu_{\text{O}}$ ). Plausible domain boundaries of additional two-phase regions [dotted lines in Fig. 4(b)] were drawn using the same phase assemblages, as shown in more detail in Sec. S4 [51].

Summarizing, this study demonstrates that the surface of LSMO(110) is sensitive to both cation composition and  $\mu_{\text{O}}$ , which determine the appearance and/or coexistence of complex surface reconstructions. The behavior witnessed is rich, and agrees with the Gibbs' phase rule, as showcased here for the surface of a multielement oxide. The surfaces of other multielement oxides with easily reducible cations are expected to behave similarly.

This work advances the knowledge needed to control complex-oxide surfaces: It demonstrates how to quantify surface cation concentrations using phase separations, and how to experimentally establish quantitative phase diagrams that organize the multitude of structures intrinsic to complex-oxide surfaces. Importantly, it directs one towards the conditions needed to prepare desired surface phases.

This work was supported by the Vienna Science and Technology Fund (WWTF), the City of Vienna and Bernsdorf Privatstiftung through project MA 16-005. The authors were supported by the Austrian Science Foundation (FWF)

through the special research projects (SFB) F81 “Taming complexity in materials modeling” (TACO) and F45 (FOXSI). G.F. acknowledges support by the Doctoral School TU-D of the TU Wien.

- [1] S. Surnev, M. G. Ramsey, and F. P. Netzer, Vanadium oxide surface studies, *Prog. Surf. Sci.* **73**, 117 (2003).
- [2] F. Li, G. Parteder, F. Allegretti, C. Franchini, R. Podloucky, S. Surnev, and F. P. Netzer, Two-dimensional manganese oxide nanolayers on Pd(100): The surface phase diagram, *J. Phys.: Condens. Matter* **21**, 134008 (2009).
- [3] F. Sedona, G. A. Rizzi, S. Agnoli, F. X. Llabrés i Xamena, A. Papageorgiou, D. Ostermann, M. Sambì, P. Finetti, K. Schierbaum, and G. Granozzi, Ultrathin  $\text{TiO}_x$  films on Pt(111): A LEED, XPS, and STM investigation, *J. Phys. Chem. B* **109**, 24411 (2005).
- [4] S. Shaikhutdinov and H.-J. Freund, Ultrathin oxide films on metal supports: Structure-reactivity relations, *Annu. Rev. Phys. Chem.* **63**, 619 (2012).
- [5] F. P. Netzer, “Small and beautiful”—The novel structures and phases of nano-oxides, *Surf. Sci.* **604**, 485 (2010).
- [6] R. Shimizu, K. Iwaya, T. Ohsawa, S. Shiraki, T. Hasegawa, T. Hashizume, and T. Hitosugi, Effect of oxygen deficiency on  $\text{SrTiO}_3(001)$  surface reconstructions, *Appl. Phys. Lett.* **100**, 263106 (2012).
- [7] Z. Wang, A. Loon, A. Subramanian, S. Gerhold, E. McDermott, J. A. Enterkin, M. Hieckel, B. C. Russell, R. J. Green, A. Moewes, J. Guo, P. Blaha, M. R. Castell, U. Diebold, and L. D. Marks, Transition from reconstruction toward thin film on the (110) surface of strontium titanate, *Nano Lett.* **16**, 2407 (2016).
- [8] G. Franceschi, M. Schmid, U. Diebold, and M. Riva, Atomically resolved surface phases of  $\text{La}_{0.8}\text{Sr}_{0.2}\text{MnO}_3(110)$  thin films, *J. Mater. Chem. A* **8**, 22947 (2020).
- [9] C. Noguera, Polar oxide surfaces, *J. Phys.: Condens. Matter* **12**, R367 (2000).
- [10] K. Reuter and M. Scheffler, Composition, structure, and stability of  $\text{RuO}_2(110)$  as a function of oxygen pressure, *Phys. Rev. B* **65**, 035406 (2001); entropy and enthalpy were taken from Ref. [59].
- [11] G. Franceschi, M. Wagner, J. Hofinger, T. Krajić, M. Schmid, U. Diebold, and M. Riva, Growth of  $\text{In}_2\text{O}_3(111)$  thin films with optimized surfaces, *Phys. Rev. Mater.* **3**, 103403 (2019).
- [12] Z. Wang, X. Hao, S. Gerhold, M. Schmid, C. Franchini, and U. Diebold, Vacancy clusters at domain boundaries and band bending at the  $\text{SrTiO}_3(110)$  surface, *Phys. Rev. B* **90**, 035436 (2014).
- [13] W. J. I. DeBenedetti, E. S. Skibinski, D. Jing, A. Song, and M. A. Hines, Atomic-scale understanding of catalyst activation: Carboxylic acid solutions, but not the acid itself, increase the reactivity of anatase (001) faceted nanocatalysts, *J. Phys. Chem. C* **122**, 4307 (2018).
- [14] M. E. McBriarty, J. E. Stubbs, P. J. Eng, and K. M. Rosso, Potential-specific structure at the hematite–electrolyte interface, *Adv. Funct. Mater.* **28**, 1705618 (2018).
- [15] Y. Pan, C. Zhang, Z. Liu, C. Chen, and Y. Li, Structural regulation with atomic-level precision: From single-atomic site to diatomic and atomic interface catalysis, *Matter* **2**, 78 (2020).
- [16] Z. Jakub, F. Kraushofer, M. Bichler, J. Balajka, J. Hulva, J. Pavelec, I. Sokolović, M. Müllner, M. Setvin, M. Schmid *et al.*, Partially dissociated water dimers at the water–hematite interface, *ACS Energy Lett.* **4**, 390 (2019).
- [17] Z. Jakub, J. Hulva, M. Meier, R. Bliem, F. Kraushofer, M. Setvin, M. Schmid, U. Diebold, C. Franchini, and G. S. Parkinson, Local structure and coordination define adsorption in a model  $\text{Ir}_1/\text{Fe}_3\text{O}_4$  single-atom catalyst, *Angew. Chem.* **131**, 14099 (2019).
- [18] M. Riva, M. Kubicek, X. Hao, G. Franceschi, S. Gerhold, M. Schmid, H. Hutter, J. Fleig, C. Franchini, B. Yildiz, and U. Diebold, Influence of surface atomic structure demonstrated on oxygen incorporation mechanism at a model perovskite oxide, *Nat. Commun.* **9**, 3710 (2018).
- [19] Y. Zhu, P. A. Salvador, and G. S. Rohrer, Controlling the relative areas of photocathodic and photoanodic terraces on the  $\text{SrTiO}_3(111)$  surface, *Chem. Mater.* **28**, 5155 (2016).
- [20] R. Qin, K. Liu, Q. Wu, and N. Zheng, Surface coordination chemistry of atomically dispersed metal catalysts, *Chem. Rev.* **120**, 11810 (2020).
- [21] P. Zubko, S. Gariglio, M. Gabay, P. Ghosez, and J.-M. Triscone, Interface physics in complex oxide heterostructures, *Annu. Rev. Condens. Matter Phys.* **2**, 141 (2011).
- [22] A. S. Bhalla, R. Guo, and R. Roy, The perovskite structure—a review of its role in ceramic science and technology, *Mater. Res. Innovations* **4**, 3 (2000).
- [23] M. A. Peña and J. L. G. Fierro, Chemical structures and performance of perovskite oxides, *Chem. Rev.* **101**, 1981 (2001).
- [24] D. P. Kumah, J. H. Ngai, and L. Kornblum, Epitaxial oxides on semiconductors: From fundamentals to new devices, *Adv. Funct. Mater.* **30**, 1901597 (2020).
- [25] S. Majumdar and S. van Dijken, Pulsed laser deposition of  $\text{La}_{1-x}\text{Sr}_x\text{MnO}_3$ : Thin-film properties and spintronic applications, *J. Phys. D: Appl. Phys.* **47**, 034010 (2013).
- [26] J.-H. Park, E. Vescovo, H.-J. Kim, C. Kwon, R. Ramesh, and T. Venkatesan, Direct evidence for a half-metallic ferromagnet, *Nature (London)* **392**, 794 (1998).
- [27] A. M. Haghiri-Gosnet, T. Arnal, R. Soulimane, M. Koubaa, and J. P. Renard, Spintronics: perspectives for the half-metallic oxides, *Phys. Status Solidi A* **201**, 1392 (2004).
- [28] J. Hwang, R. R. Rao, L. Giordano, Y. Katayama, Y. Yu, and Y. Shao-Horn, Perovskites in catalysis and electrocatalysis, *Science* **358**, 751 (2017).
- [29] S. Ponce, M. A. Peña, and J. L. G. Fierro, Surface properties and catalytic performance in methane combustion of Sr-substituted lanthanum manganites, *Appl. Catal. B* **24**, 193 (2000).
- [30] S. P. Jiang, Development of lanthanum strontium manganese perovskite cathode materials of solid oxide fuel cells: A review, *J. Mater. Sci.* **43**, 6799 (2008).
- [31] J. C. Ruiz-Morales, D. Marrero-López, J. Canales-Vázquez, and J. T. S. Irvine, Symmetric and reversible solid oxide fuel cells, *RSC Adv.* **1**, 1403 (2011).

- [32] Z. Liao and J. Zhang, Metal-to-insulator transition in ultrathin manganite heterostructures, *Appl. Sci.* **9**, 144 (2019).
- [33] J. Huang, H. Wang, X. Sun, X. Zhang, and H. Wang, Multifunctional  $\text{La}_{0.67}\text{Sr}_{0.33}\text{MnO}_3$  (LSMO) thin films integrated on mica substrates toward flexible spintronics and electronics, *ACS Appl. Mater. Interfaces* **10**, 42698 (2018).
- [34] B.-C. Huang, P. Yu, Y. H. Chu, C.-S. Chang, R. Ramesh, R. E. Dunin-Borkowski, P. Ebert, and Y.-P. Chiu, Atomically resolved electronic states and correlated magnetic order at termination engineered complex oxide heterointerfaces, *ACS Nano* **12**, 1089 (2018).
- [35] Q. Li, Y.-X. Deng, Y.-A. Zhu, Y. Li, Z.-J. Sui, D. Chen, and W.-K. Yuan, Structural stability of lanthanum-based oxygen-deficient perovskites in redox catalysis: A density functional theory study, *Catal. Today* **347**, 142 (2020).
- [36] J. Hemberger, A. Krimmel, T. Kurz, H.-A. Krug von Nidda, V. Y. Ivanov, A. A. Mukhin, A. M. Balbashov, and A. Loidl, Structural, magnetic, and electrical properties of single-crystalline  $\text{La}_{1-x}\text{Sr}_x\text{MnO}_3$  ( $0.4 < x < 0.85$ ), *Phys. Rev. B* **66**, 094410 (2002).
- [37] Y. Shirai, S. Hashimoto, K. Sato, K. Yashiro, K. Amezawa, J. Mizusaki, and T. Kawada, Crystal structure and thermal expansion behavior of oxygen stoichiometric lanthanum strontium manganite at high temperature, *Solid State Ionics* **256**, 83 (2014).
- [38] Y.-M. Kim, J. He, M. D. Biegalski, H. Ambaye, V. Lauter, H. M. Christen, S. T. Pantelides, S. J. Pennycook, S. V. Kalinin, and A. Y. Borisevich, Probing oxygen vacancy concentration and homogeneity in solid-oxide fuel-cell cathode materials on the subunit-cell level, *Nat. Mater.* **11**, 888 (2012).
- [39] S. B. Adler, Factors governing oxygen reduction in solid oxide fuel cell cathodes, *Chem. Rev.* **104**, 4791 (2004).
- [40] N. C. Bristowe, P. B. Littlewood, and E. Artacho, Surface defects and conduction in polar oxide heterostructures, *Phys. Rev. B* **83**, 205405 (2011).
- [41] J. Chen, H. Arandiyani, X. Gao, and J. Li, Recent advances in catalysts for methane combustion, *Catal. Surv. Asia* **19**, 140 (2015).
- [42] J. Fan, Y. Xie, Y. Zhu, F. Qian, Y. Ji, D. Hu, W. Tong, L. Zhang, L. Ling, C. Wang *et al.*, Emergent phenomena of magnetic skyrmion and large DM interaction in perovskite manganite  $\text{La}_{0.8}\text{Sr}_{0.2}\text{MnO}_3$ , *J. Magn. Magn. Mater.* **483**, 42 (2019).
- [43] T. K. Andersen, D. D. Fong, and L. D. Marks, Pauling's rules for oxide surfaces, *Surf. Sci. Rep.* **73**, 213 (2018).
- [44] J. A. Enterkin, A. K. Subramanian, B. C. Russell, M. R. Castell, K. R. Poeppelmeier, and L. D. Marks, A homologous series of structures on the surface of  $\text{SrTiO}_3(110)$ , *Nat. Mater.* **9**, 245 (2010).
- [45] S. Gerhold, Z. Wang, M. Schmid, and U. Diebold, Stoichiometry-driven switching between surface reconstructions on  $\text{SrTiO}_3(001)$ , *Surf. Sci.* **621**, L1 (2014).
- [46] J. Feng, X. Zhu, and J. Guo, Reconstructions on  $\text{SrTiO}_3(111)$  surface tuned by Ti/Sr deposition, *Surf. Sci.* **614**, 38 (2013).
- [47] Y. A. Mastrikov, E. Heifets, E. A. Kotomin, and J. Maier, Atomic, electronic and thermodynamic properties of cubic and orthorhombic  $\text{LaMnO}_3$  surfaces, *Surf. Sci.* **603**, 326 (2009).
- [48] Y. Li, J. Yang, Y.-A. Zhu, Z.-J. Sui, X.-G. Zhou, D. Chen, and W.-K. Yuan, Surface phase diagrams of La-based perovskites towards the O-rich limit from first principles, *Phys. Chem. Chem. Phys.* **21**, 12859 (2019).
- [49] F. Hess and B. Yildiz, Polar or not polar? The interplay between reconstruction, Sr enrichment, and reduction at the  $\text{La}_{0.75}\text{Sr}_{0.25}\text{MnO}_3(001)$  surface, *Phys. Rev. Mater.* **4**, 015801 (2020).
- [50] S. Gerhold, M. Riva, B. Yildiz, M. Schmid, and U. Diebold, Adjusting island density and morphology of the  $\text{SrTiO}_3(110)$ - $(4 \times 1)$  surface: Pulsed laser deposition combined with scanning tunneling microscopy, *Surf. Sci.* **651**, 76 (2016).
- [51] See Supplemental Material at <http://link.aps.org/supplemental/10.1103/PhysRevMaterials.5.L092401> for further experimental details (Sec. S1), an overview of the high-pressure (Sec. S2) and low-pressure (Sec. S3) surface structures of  $\text{LSMO}(110)$ , an in-depth description of the steps taken to build the 2D surface phase diagram (Sec. S4), as well as considerations concerning the oxidation state of Mn at the surface (Sec. S5), which includes Refs. [60–70].
- [52] M. Kubicek, G. M. Rupp, S. Huber, A. Penn, A. K. Opitz, J. Bernardi, M. Stöger-Pollach, H. Hutter, and J. Fleig, Cation diffusion in  $\text{La}_{0.6}\text{Sr}_{0.4}\text{CoO}_{3-\delta}$  below  $800^\circ\text{C}$  and its relevance for Sr segregation, *Phys. Chem. Chem. Phys.* **16**, 2715 (2014).
- [53] M. Riva, G. Franceschi, M. Schmid, and U. Diebold, Epitaxial growth of complex oxide films: Role of surface reconstructions, *Phys. Rev. Res.* **1**, 033059 (2019).
- [54] A. T. Kozakov, A. G. Kochur, K. A. Googlev, A. V. Nikolskii, V. I. Torgashev, V. G. Trotsenko, and A. A. Bush, Valence state of manganese and iron ions in  $\text{La}_{1-x}\text{A}_x\text{MnO}_3$  ( $\text{A} = \text{Ca}, \text{Sr}$ ) and  $\text{Bi}_{1-x}\text{Sr}_x\text{FeO}_3$  systems from Mn  $2p$ , Mn  $3s$ , Fe  $2p$  and Fe  $3s$  x-ray photoelectron spectra. Effect of delocalization on Fe  $3s$  spectra splitting, *J. Alloys Compd.* **647**, 947 (2015).
- [55] M. Abbate, F. M. F. de Groot, J. C. Fuggle, A. Fujimori, O. Strebel, F. Lopez, M. Domke, G. Kaindl, G. A. Sawatzky, M. Takano, Y. Takeda, H. Eisaki, and S. Uchida, Controlled-valence properties of  $\text{La}_{1-x}\text{Sr}_x\text{FeO}_3$  and  $\text{La}_{1-x}\text{Sr}_x\text{MnO}_3$  studied by soft-x-ray absorption spectroscopy, *Phys. Rev. B* **46**, 4511 (1992).
- [56] T. Saitoh, A. E. Bocquet, T. Mizokawa, H. Namatame, A. Fujimori, M. Abbate, Y. Takeda, and M. Takano, Electronic structure of  $\text{La}_{1-x}\text{Sr}_x\text{MnO}_3$  studied by photoemission and x-ray-absorption spectroscopy, *Phys. Rev. B* **51**, 13942 (1995).
- [57] A. M. Kolpak, D. Li, R. Shao, A. M. Rappe, and D. A. Bonnell, Evolution of the Structure and Thermodynamic Stability of the  $\text{BaTiO}_3(001)$  Surface, *Phys. Rev. Lett.* **101**, 036102 (2008).
- [58] A. Tselev, R. K. Vasudevan, A. G. Gianfrancesco, L. Qiao, P. Ganesh, T. L. Meyer, H. N. Lee, M. D. Biegalski, A. P. Baddorf, and S. V. Kalinin, Surface control of epitaxial manganite films via oxygen pressure, *ACS Nano* **9**, 4316 (2015).
- [59] M. W. Chase, Jr., C. A. Davies, J. R. Downey, Jr., D. J. Frurip, R. A. McDonald, and A. N. Syverud, *NIST-JANAF Thermochemical Tables* (National Institute of Standards and Technology, Gaithersburg, MD, 1998).
- [60] Y. Yao and K. P. Giapis, Tuning charge transfer in ion-surface collisions at hyperthermal energies, *Chem. Phys. Chem.* **17**, 1430 (2016).
- [61] M. Riva, G. Franceschi, Q. Lu, M. Schmid, B. Yildiz, and U. Diebold, Pushing the detection of cation nonstoichiometry to the limit, *Phys. Rev. Mater.* **3**, 043802 (2019).
- [62] D. S. Mebane, Y. Liu, and M. Liu, Refinement of the bulk defect model for  $\text{La}_x\text{Sr}_{1-x}\text{MnO}_{3\pm\delta}$ , *Solid State Ionics* **178**, 1950 (2008).

- [63] S. H. Albedwawi, A. AlJaberi, G. N. Haidemenopoulos, and K. Polychronopoulou, High entropy oxides—exploring a paradigm of promising catalysts: A review, *Mater. Des.* **202**, 109534 (2021).
- [64] A. D. Pelton, *Phase Diagrams and Thermodynamic Modeling of Solutions* (Elsevier, Amsterdam, 2019).
- [65] E. S. Domalski and E. D. Hearing, Condensed phase heat capacity data, in *NIST Chemistry WebBook, NIST Standard Reference Database Number 69*, edited by P. J. Linstrom and W. G. Mallard (National Institute of Standards and Technology, Gaithersburg, MD).
- [66] A. Manzoor and D. S. Aidhy, Predicting vibrational entropy of fcc solids uniquely from bond chemistry using machine learning, *Materialia* **12**, 100804 (2020).
- [67] E. Beyreuther, S. Grafström, L. M. Eng, C. Thiele, and K. Dörr, XPS investigation of Mn valence in lanthanum manganite thin films under variation of oxygen content, *Phys. Rev. B* **73**, 155425 (2006).
- [68] M. P. de Jong, I. Bergenti, V. A. Dediu, M. Fahlman, M. Marsi, and C. Taliani, Evidence for  $\text{Mn}^{2+}$  ions at surfaces of  $\text{La}_{0.7}\text{Sr}_{0.3}\text{MnO}_3$  thin films, *Phys. Rev. B* **71**, 014434 (2005).
- [69] K. A. Stoerzinger, M. Risch, J. Suntivich, W. M. Lü, J. Zhou, M. D. Biegalski, H. M. Christen, Ariando, T. Venkatesan, and Y. Shao-Horn, Oxygen electrocatalysis on (001)-oriented manganese perovskite films: Mn valency and charge transfer at the nanoscale, *Energy Environ. Sci.* **6**, 1582 (2013).
- [70] P. Lackner, Z. Zou, S. Mayr, U. Diebold, and M. Schmid, Using photoelectron spectroscopy to observe oxygen spillover to zirconia, *Phys. Chem. Chem. Phys.* **21**, 17613 (2019).